Eur. Phys. J. C 5, 63–75 (1998)
DOI 10.1007/s100529800892

THE EUROPEAN PHYSICAL JOURNAL C

Study of vector mesons in dimuon production in a large kinematic region in p–W and S–W interactions at 200 GeV/c/nucleon

The HELIOS/3 collaboration

A.L.S. Angelis[2,a], J. Antos[3], M. Beaulieu[4], H. Beker[2], G. Briskin[2,b], J. Bystricky[8], M.-G. Catanesi[1], P. Cerello[9], S. Dagan[2,c], G. Dellacasa[9], M. Diehl[8], S. Di Liberto[7], B. Dolgoshein[5], M. Esten[2,d], C.W. Fabjan[2], A. Gaidot[8], M. Gallio[1], P. Giubellino[9], U. Goerlach[2], C. Guerra[8], L.-A. Hamel[4], S. Konovalov[6], I. Kralik[3], G. London[8], F. Martelli[9], J.-P. Martin[4] M. Masera[9], M.-A. Mazzoni[7], F. Meddi[7], M.-T. Muciaccia[1], S. Muraviev[6], A. Nomerotsky[2], Y. Oren[2,e], J.-P. Pansart[8], G. Poulard[2], L. Ramello[9], L. Riccati[9], G. Rosa[7], L. Sandor[3], M. Sarris[2], E. Scomparin[9], A. Shmeleva[6], S. Simone[1], S. Smirnov[5], P. Taras[4], J. Urban[3], E. Vercellin[9]

[1] University of Bari and INFN, Bari, Italy
[2] CERN, CH-1211 Geneva, Switzerland
[3] Slovak Academy of Sciences, Kosice, Slovak Republic
[4] University of Montreal, Montreal, Canada
[5] Lebedev Institute of Physics, Moscow, Russia
[6] Institute of Physics and Engineering, Moscow, Russia
[7] University of Rome "La Sapienza" and INFN Rome, Italy
[8] DAPNIA, CE-Saclay, Gif/Yvette, France
[9] University of Turin and INFN Turin, Italy

Received: 27 October 1997 / Revised version: 5 March 1998 / Published online: 13 July 1998

Abstract. Results are presented on $\rho + \omega, \phi$ and J/Ψ production in p–W and ^{32}S–W interactions at 200 GeV/c/nucleon measured via the dimuon decay in a large kinematic region. The data are normalized to the charged particle multiplicity in the same rapidity interval. They have been collected using the HELIOS/3 muon spectrometer at the CERN SPS. The ratio $B\sigma_\phi/(B\sigma_\rho + B\sigma_\omega)$, where B is the relevant resonance $\mu\mu$ branching fraction, increases between proton and sulphur projectiles, and is somewhat enhanced going from peripheral to central S–W interactions. This results from an increase in the number of produced ϕ's per charged particle. The ratio is measured in different intervals of p_T and rapidity. It is not clearly dependent on p_T, but is larger at higher rapidities. J/Ψ production, likewise normalized to charged multiplicity, is significantly lower in S–W compared to p–W interactions.

1 Introduction

The study of vector meson production in the environment of large hadron densities achieved in interactions of ultrarelativistic ions can be used to probe phenomena such as chiral symmetry restoration, strangeness enhancement and J/Ψ suppression in a quark gluon plasma (QGP). In the limit of chiral symmetry restoration, the quark masses tend to zero and consequently vector meson masses and widths should change. In-medium effects in hot or dense nuclear matter like a hadron gas can also strongly shift the effective mass of the ρ resonance [1–4].

Rafelski and Muller [5] have suggested that a quark-gluon plasma created in nuclear interactions would result in an enhanced production of strange quarks. In this picture, the enhancement is due to the large number of gluons which are responsible for a fast rate of flavor equilibration. The measurement of the ratio $B\sigma_\phi/(B\sigma_\rho + B\sigma_\omega)$ is a way to study an enhancement of strangeness production [6]. The ϕ and ω are identical in their quantum numbers and are comparable in mass; they differ primarily in their quark content. The $\sigma_\phi/\sigma_\omega$ ratio in p–p interactions is $\approx 5\%$ [7]. In S–W interactions, it could be as large as 1 [6]. Another estimation including hadronic absorption but no QGP [8] predicts a smaller enhancement of this ratio, but still 6–10 times its p–p value. The latter analysis links the observation of ϕ enhancement and J/Ψ suppression.

[a] also McGill University, Montreal,Canada
[b] presently at Tel Aviv University, Tel Aviv, Israel
[c] also Saclay; on leave of absence from Tel Aviv University, Tel Aviv, Israel
[d] also University College, London, Great Britain
[e] on leave of absence from Tel Aviv University, Tel Aviv, Israel

Finally, another hadronic model [9] with no QGP but with final state absorption predicts a factor of two increase of the ratios ρ/π and ϕ/π and a 40% decrease of ω/π, going from p–p to central S–W interactions.

The HELIOS/3 experiment at the CERN SPS was designed to explore the especially interesting spectrum of low mass and low transverse momentum dimuons as well as the relative production of vector mesons ϕ, ρ, and ω in a large kinematic region.

In this article, we present our measurements of the ϕ, $\rho + \omega$ and J/Ψ vector mesons, normalized to the charged particles produced in approximately the same pseudorapidity acceptance. The data are presented as a function of transverse momentum, rapidity and centrality, the latter estimated by the accompanying charged multiplicity [10].

2 Experimental set-up and trigger

The experimental configuration, which was installed in the H8-beam line of the CERN SPS, is shown in Fig. 1 [10]. The target region with beam counters, silicon ring counters and a petal hodoscope is detailed in the inset. The Z-axis of our right-handed coordinate system coincides with the beam direction, while the Y-axis is oriented vertically.

The beam signal was defined by an anti-coincidence of the veto counters, LV and SV, with the beam scintillators LB and SB, or alternatively with the quartz counter Q and scintillator LB for protons and sulphur projectiles, respectively (inset in Fig. 1). A gas threshold Čerenkov counter in the beam line was used to veto pions during the proton running. The six scintillators of the petal hodoscope covering the pseudorapidity region $1.8 \leq \eta \leq 3.9$ provided the interaction trigger referred to as "INT" in the following. At least 3 counters of the hodoscope were required, each being hit by 1 or by 5 to 6 particles in proton or in sulphur runs, respectively.

The use of silicon counters SiR_1 and SiR_2 was twofold. They provided a fast trigger on the charged multiplicity and detailed off-line information on the charged particle multiplicity of the event. Within the rigorously reduced space allowed for π and K decays in front of the absorber, the lay-out of the silicon pad detectors was optimized to measure the flux of particles strongly increasing in the forward rapidity region. The first counter SiR_1 consisted of 384 pads in 12 sectors covering the pseudorapidity region of $1.6 \leq \eta \leq 3.7$; the second one SiR_2, with 288 pads in 24 sectors, covered the region of $2.6 \leq \eta \leq 5.5$.

The multiplicity signal in the inner part of SiR_2, ($3.7 \leq \eta \leq 5.5$, approximately the muon spectrometer acceptance), was used as a trigger condition to select the centrality of the events. Three discrimination levels on the digital Si multiplicity were used in the sulphur runs to enhance the number of central event triggers; they correspond to the beginning of the plateau, the knee and the tail of the multiplicity distribution (Fig. 2). As seen previously [11], the correlation of hits in the two silicon counters (Fig. 3) demonstrates the proportionality of the forward and mid-rapidity multiplicities for low multiplicity values and a saturation of the forward multiplicity for very central events. In addition, events triggered by the interaction trigger signal ("INT") alone were also recorded ($\sim$ minimum bias trigger).

A tungsten rod target of 1 mm diameter and of 5 or 10 mm length for sulphur or proton runs, respectively, was placed 25 cm before the hadron absorber. The two target lengths correspond to about 13% of an interaction length using the S–W inelastic cross section and about 12% of an interaction length using the p–W inelastic cross section. The absorber was optimized for low transverse mass dimuon measurements and consisted of an Al_2O_3 cone 180 cm long (6 interaction lengths) followed by 100 cm of iron (6 interaction lengths). An 8 mrad conic hole centered on the beam axis, followed by a 60 cm long tungsten rod starting at 146 cm from the target, insured that most ion fragments interacted far from the target.

The large acceptance muon spectrometer consisted of a dipole magnet with a vertical field of 4.1 Tm and 7 multiwire proportional chambers for a total of 32 X, Y, U, V planes. A scintillator hodoscope H1 was placed at the exit of the magnet; after the last chamber, an 80 cm iron hadron filter was sandwiched between two trigger hodoscopes H3 and H2. Except for the addition of H1 consisting of 14 $2\times0.15\,m^2$ slabs, the configuration of the spectrometer was identical to the one used in the HELIOS/1 experiment [12].

Each hodoscope, H3 and H2, was made up of two layers of scintillators, Front and Back. Each layer consisted of several rows in the (vertical) Y direction, and each row contained two (Left and Right) horizontal scintillator slabs. H3 and H2 were vertically offset by 1/2 slab height.

H3 and H2 provided the first-level dimuon trigger. Trigger rows were defined in each hodoscope by an 'OR' of the 4 slabs: Front/Left, Front/Right, Back/Left, Back/Right, except for the two rows in H3 immediately above and below the beam axis where the Left and Right slabs were not 'ORed'. The muon first-level trigger required at least two coincidences between H3 and H2, a hit in an H3 row to be in coincidence with a hit in either of the H2 rows which overlap with it. The dimuon trigger was completed at the second level by requiring the reconstruction of at least two X-Z track projections in chambers PC3, PC5 and PC6. To eliminate events which are difficult to reconstruct, dimuon triggers were eliminated for most of the sulphur runs when more than six of the 11 slabs of H1 fired. A small multiplicity-dependent correction was determined from the runs with no anti-coincidence condition.

To summarize, our dimuon trigger was defined by

$$(H2 \cdot H3 \geq 2) \cdot (PC3/5/6 \geq 2)$$

for the proton and the first part of the sulphur running, and

$$(H2 \cdot H3 \geq 2) \cdot (PC3/5/6 \geq 2) \cdot \overline{(H1 > 6)}$$

for the second (larger) part of the sulphur running. It was used in coincidence with a multiplicity requirement, either

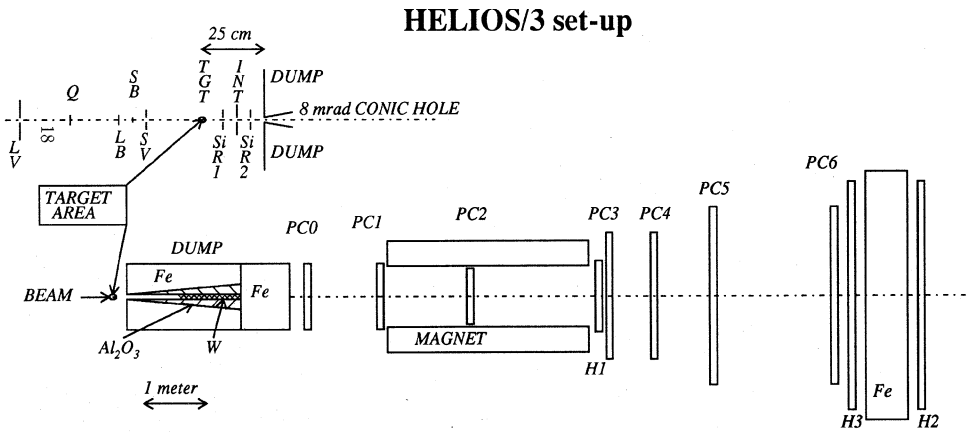

Fig. 1. Overall experimental setup with target region inset

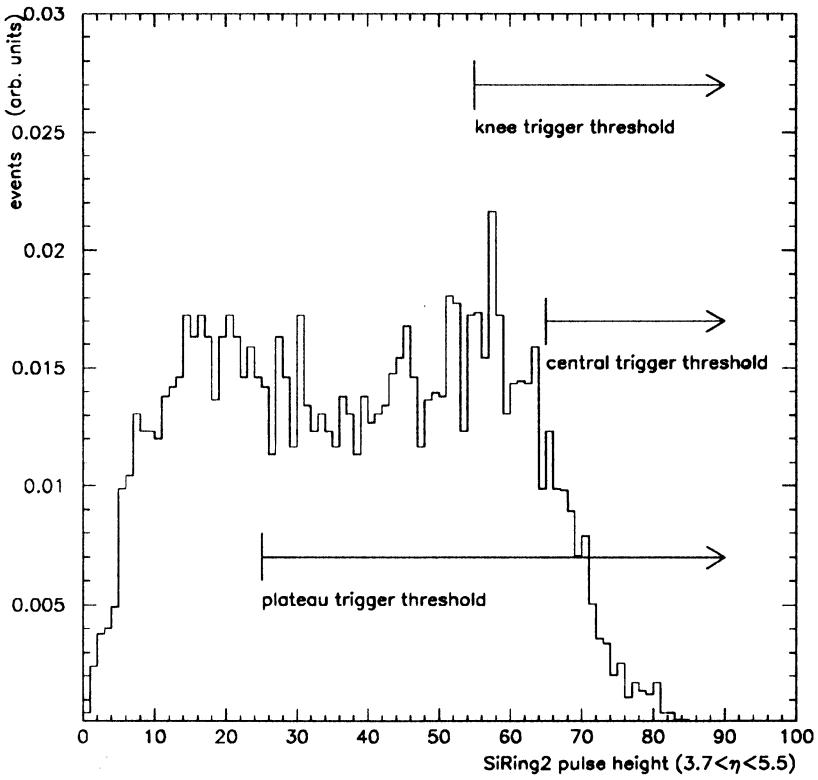

Fig. 2. Silicon ring trigger pulse height distribution and the three trigger thresholds

using the interaction signal or a signal based on the second silicon ring counter, with $3.7 \leq \eta \leq 5.5$. We define a 2μ event trigger as the dimuon trigger together with its multiplicity requirement. In parallel, we accumulated events defined by the multiplicity trigger only, labeled 0μ, appropriately downscaled.

3 Data reduction and analysis

During nineteen days of data taking in 1990 with the 200 GeV/c sulphur beam and the tungsten target we collected 9×10^6 dimuon triggers. This number was reduced to 3.2×10^5 events by requiring a clean sulphur beam signal, compatibility of the information from the two silicon ring detectors and exactly two reconstructed tracks in the spectrometer. This large reduction is detailed as follows. Requiring at least 2 reconstructed tracks reduces the triggers to about 40% of the original number. The correspondence of an H2/H3 coincidence with a charged track defines a muon. The requirement that exactly 2 muons are identified reduced the triggers by about a factor 10. (It should be pointed out that the chamber wires and the hodoscope slabs were orthogonal.) The percentage of events with 3 or more identified muons was about 7% in the sulphur sample, and less in the proton sample.

The target selection by vertex cuts, and a restricted kinematic region (see section below on acceptance) decreased the number to 2.7×10^5 dimuon events used in the analysis, of which 68.4% were $\mu^+\mu^-$, 14.4% $\mu^+\mu^+$ and 17.2% $\mu^-\mu^-$. Similar selection criteria resulted in 44200 dimuon events for the proton beam run with 95.6% $\mu^+\mu^-$, 3.3% $\mu^+\mu^+$ and 1.1% $\mu^-\mu^-$ pairs. Note that the separa-

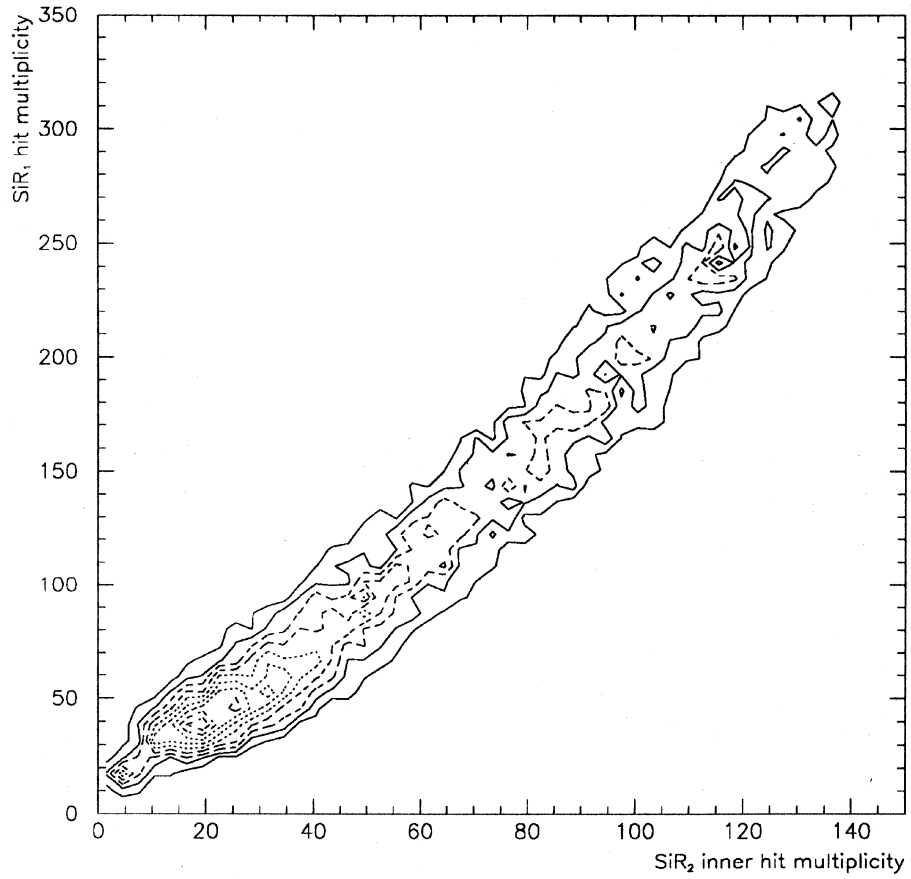

Fig. 3. Mid-rapidity multiplicity ($1.6 < \eta < 3.7$; SiR_1) vs. forward multiplicity ($3.5\eta < 5.2$; inner SiR_2) in S–W interactions. Notice that the forward multiplicity begins to saturate at high multiplicity

tion into Left and Right of the two H3 rows nearest the beam axis made a significant reduction in number of like-sign dimuons at low transverse momentum. The resulting trigger bias was removed in the analysis. Note also that the proton beam produces more $\mu^+\mu^+$ than $\mu^-\mu^-$, reflecting the quark content of the projectile, while the numbers are approximately equal for the sulphur beam.

3.1 Beam selection

The information from the various beam counters was used off-line to reject events from ions other than sulphur as well as pile-up events. A multihit TDC recorded the arrival time of beam particles neighboring the one which caused the trigger. Events were kept when no other particle was found closer than 40 ns before or 300 ns after the trigger. The fraction of events rejected varies from 7 to 15% depending on the beam intensity. The quartz counter and the LB scintillator information were combined in order to define the incoming beam charge. First a correction for the pulse-height dependence on the beam intensity was applied to both counters. The pulse-heights of the two counters were then normalized and averaged, with a resolution ranging from 5 to 7%. The sulphur beam was defined by a 3 sigma cut around the peak of the weighted mean; about 5% of the events, mainly residual pile-up, were rejected. We could not separate S^{16+} from P^{15+}, however the latter contamination appears negligible in the analyzed sample.

3.2 Interaction clean-up

Information from the 2 silicon ring counters was used to reduce the contamination due to interactions occurring out of the target. A very good correlation in the hit multiplicity between the two counters is expected in the events originating from the target. In our data, a small fraction of the events ($\simeq$ 1%) showed a high multiplicity in the second counter and a very small multiplicity in the first. These events were eliminated since they were probably due to interactions in the first ring counter.

Events from upstream interactions were rejected by a cut on the pattern correlation between the two counters. The cut was defined by looking at data taken with and without the target and then verified with a simple geometrical Monte Carlo program. This procedure removed $\simeq$ 3% of the events.

3.3 Track reconstruction

Track reconstruction begins behind the magnet (chambers PC3–6) by finding two straight lines in each of the X-Z and Y-Z projections. Those projections for which the χ^2 fit probability exceeds 0.1% were then associated by using the inclined U and V planes. Hits were not shared among different projections, but the same projection can be used more than once to find tracks in space. These space tracks

were projected upstream, through the magnet, and associated to hits in PC0–PC2. Hits in these chambers can be shared by different tracks. The complete tracks were then fitted and the best fits retained. An overall $P\left(\chi^2\right) > 1\%$ cut was used. A muon candidate is a reconstructed track which, in addition, has associated H3 and H2 slabs, taking into account multiple scattering in the iron filter.

3.4 Determination of kinematic quantities

The momentum reconstructed in the spectrometer was corrected for the average energy loss in the absorber determined by a detailed simulation of the muon trajectories in the absorber using GEANT 3.14. The reconstructed angles for each muon in the spectrometer just behind the absorber are estimators of the true angles, but are greatly influenced by the multiple scattering in the absorber which produces two effects, a change in the true angle and an apparent track displacement. For tracks originating at the target (see next section), another independent estimator for each angle can be determined by extrapolating the reconstructed track to a Z-plane at which the two effects are uncorrelated; the angles were then determined from the target position and the intersection of the track with this plane. The two independent estimators were averaged.

The mass scale was calibrated for the ϕ and J/Ψ, the first being more sensitive to energy loss and the second to the central value of the magnetic field.

3.5 Target reconstruction

The Z-coordinate of the point of closest approach to the beam axis relative to the target, Z_μ, was calculated for each muon track together with its estimated error σ_{Z_μ} whose average value increases with higher Z_μ.

A problem specific to low transverse mass dimuon measurements is an apparent forward shift of the production vertex. This shift is due to the multiple scattering of muons in the absorber material: a small opening angle between the muons is more affected than a bigger one. Thus the apparent vertex shift is particularly large for dimuons of small transverse masses, see Fig. 4a. This shift is largely but not completely compensated when normalized to the error, see Fig. 4b. The phenomenon is well understood and reproduced in simulation programs.

We kept only muons satisfying the requirement, $Z_\mu/\sigma_{Z_\mu} < 3$ and $Z_\mu < 250\,\mathrm{cm}$. These criteria were effective in rejecting dimuons which did not come from the target but they were mass-dependent retaining more dimuons at higher transverse mass as can be observed in Fig. 4; the latter effect has been taken into account in the acceptance evaluation (see below).

3.6 Acceptance and resolution

The acceptance and resolution of the apparatus were extensively studied by Monte Carlo methods. A $19 \times 17 \times 13$ acceptance grid of mass, transverse momentum, and laboratory rapidity (m, p_T, y) was determined, assuming an isotropic decay angle distribution of the dimuon. This is consistent with the results of [12]. For dimuons from charm decay, the distribution depends on the mass of the dimuons; in the mass range of this paper, the distribution is approximately isotropic [13]. A pair was accepted if both muons were successfully reconstructed in the spectrometer. Intermediate points were calculated using an interpolation scheme based on the reconstructed kinematical variables of the muon pair. The difference between the generated and reconstructed values determined the resolution function. For example, the mass resolution at the ϕ and J/Ψ mesons was 82 and $90\,\mathrm{MeV/c^2}$, respectively.

The acceptance for the $\rho \to \mu\mu$ is shown in Fig. 5 as contour lines in the m_T vs. y plane. The acceptance is mainly determined by the momentum cutoff of the absorber due to energy losses and by the strength of the dipole magnet of the spectrometer. This leads to an acceptance which is mainly determined by the transverse mass m_T and the rapidity. In order to remove events with very low acceptance, we restricted ourselves to the kinematic region

$$m_T \geq 4(7 - 2y)$$

and

$$m_T \geq \sqrt{(2m_\mu)^2 + \left(\frac{2P_{min}}{\cosh y}\right)^2}$$

motivated by symmetric dimuon decays, where $P_{min} = 7.5\,\mathrm{GeV/c}$ is well above the minimum accepted momentum determined by the energy loss in the absorber and the deflection of the magnetic field. These cuts reduce the kinematic acceptance for the analysis, as indicated in the figure. The remaining events are weighted by their acceptance which varies by about a factor 6.

3.7 Multiplicity analysis

The multiplicity of charged particles measured in the pseudorapidity region $3.5 < \eta < 5.2$ was used to group our data according to their centrality. The measurement was performed starting from the number of pads having a pulse-height exceeding a threshold defined as 60% of the minimum ionizing particle signal in $300\,\mu m$ of silicon [14]. The most important factors that limited our resolution were the high occupancy ($\sim 70\%$ of the pads for central events) and the contamination due to secondary processes, mainly electron pair production in the tungsten target. The fluctuations due to the second effect play a very important role at low multiplicities.

The determination of the relationship of the raw multiplicity to the real multiplicity, event-by-event, relied on Monte Carlo methods. A good reproduction of the raw multiplicity data was obtained using VENUS 3.11 [15] as generator and GEANT 3.14 for a full detector simulation. We divided the data in classes of overall occupancy as measured by the total number of firing pads in the detector. For each class we tabulated the relationship

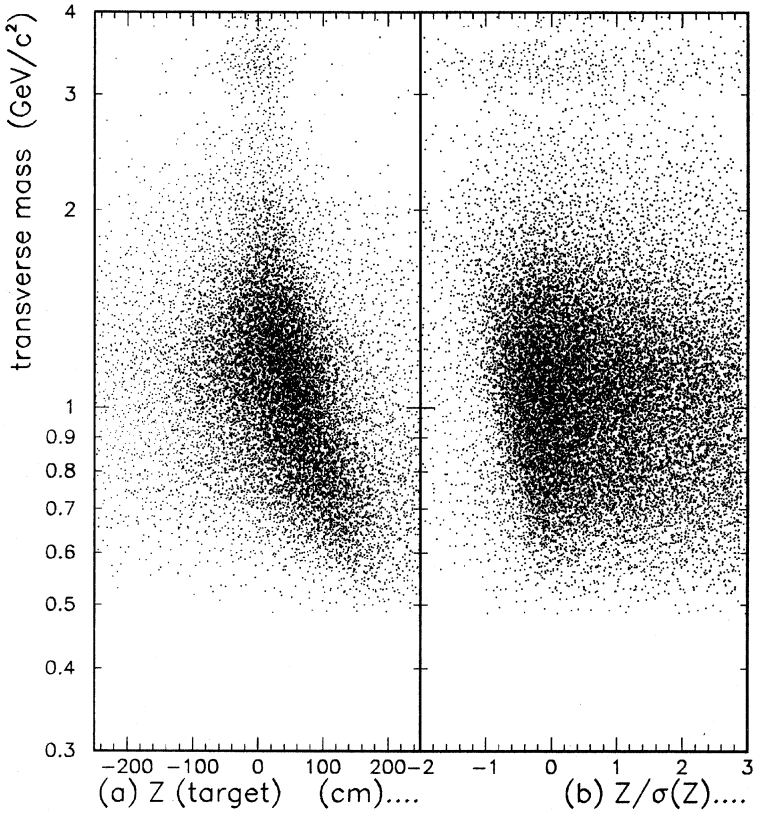

Fig. 4. Dimuon transverse mass vs. **a** reconstructed origin along beam and **b** reconstructed origin along beam normalized by its error

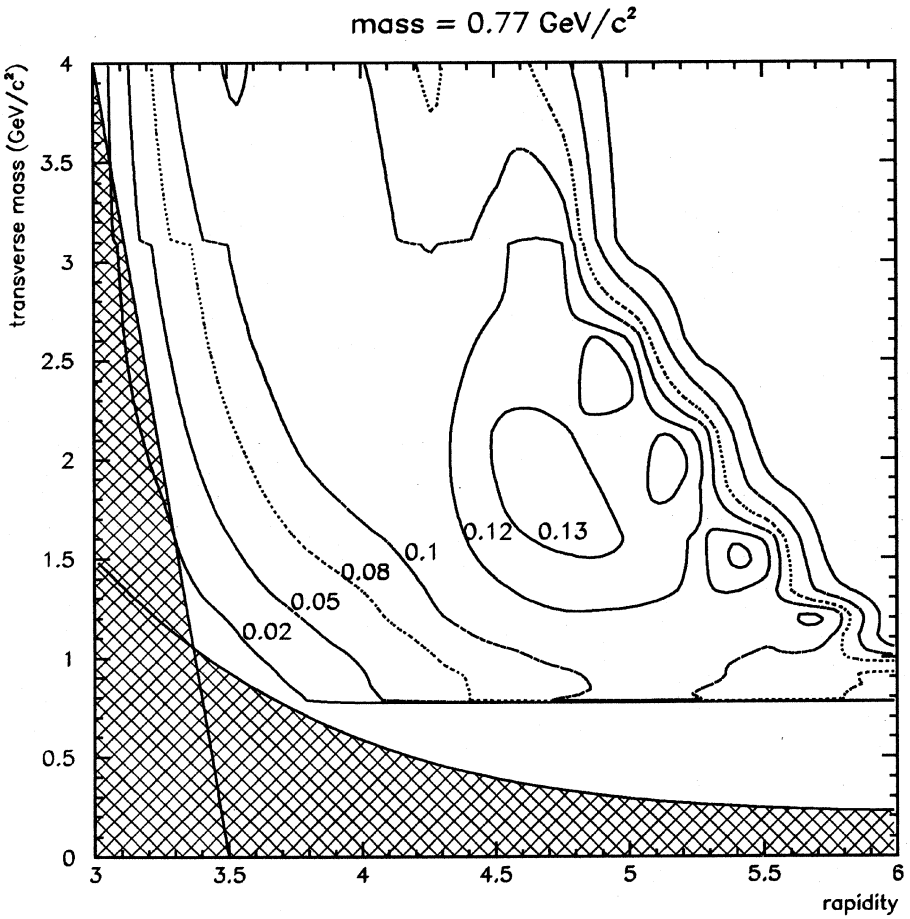

Fig. 5. Acceptance contours on the m_T vs. y plot for the central mass value of the ρ meson. The region at high rapidity and transverse mass is outside the kinematic limit

Table 1. Charged multiplicity class vs. number of projectile participants

class	multiplicity $3.5 < \eta < 5.2$	$< MULT >$	Nr. of proj. part. mean (r.m.s.)
1	$MULT \leq 25$	14.0	3.7 (3.0)
2	$25 < MULT \leq 70$	43.5	14.5 (5.6)
3	$70 < MULT \leq 100$	80.8	22.7 (5.5)
4	$100 < MULT \leq 130$	115.8	26.6 (4.8)
5	$130 < MULT \leq 160$	147.0	29.4 (2.6)
6	$160 < MULT$	165.1	30.6 (1.7)
central coll.	$100 < MULT$	134.6	28.2 (3.5)

between the number of firing pads belonging to a given ring, hence all in the same rapidity region, and the mean number of charged particles produced in the primary collision in the same region. These look-up tables were then used to correct the raw multiplicity. The achieved resolution, defined as the standard deviation of the ratio $(Mult_{corr.} - Mult_{true})/Mult_{true}$ ranged from less than 15% for very central interactions to about 50% for peripheral interactions. For protons, this value was 54%; the mean multiplicity in the p–W data was 4.6 with an RMS = 2.5. The statistical error on the mean was determined from the standard deviation and the number of events.

We grouped our data into six multiplicity classes, requiring that the triggers contributing to each class gave comparable average multiplicities. For each class, the average number of projectile participants was estimated by means of VENUS 3.11 (and checked with FRITIOF [16]). A central collision class was constructed from classes 4–6 by weighting each class with its fraction as determined by the minimum bias trigger. In Table 1 one can find the average number of projectile participants corresponding to each class. In this paper, class 1 was not used because of lack of statistics. The systematic error on the mean multiplicity was determined to be about 10% for classes 2–5 and 15% for classes 1 and 6.

3.8 Combinatorial background

An important background is due to uncorrelated muon pairs originating from π and K meson decays. Under the hypothesis that all like-sign muon pairs, N^{++} and N^{--}, are of this kind, the combinatorial background in the unlike-sign sample, N_c^{+-}, is proportional to the geometric mean of the like-sign samples with the proportionality constant defined as:

$$R \equiv N_c^{+-}/2\sqrt{N^{++}N^{--}} \quad (1)$$

The constant R depends to zeroth order on the number of positive and negative particles, tending towards unity in the limit of very large multiplicities. The precise value of R was studied extensively by a full Monte Carlo simulation, using the VENUS 3.11 generator. The result is $R = 1.14 \pm 0.02$ for the sulphur runs in all multiplicity classes, and 1.57 ± 0.10 for the proton runs. The R-value for sulphur interactions does not show a significant dependence on charged multiplicity class (since even the lowest class has a relatively high multiplicity relative to p–W interactions) nor on mass nor transverse mass. The results presented in this article are not sensitive to a change of 10% in R.

To obtain the precise shape of the combinatorial background, reducing the bin-to-bin statistical errors, we used μ pairs formed from muons in different like-sign events within the same multiplicity class. The trigger bias was first removed by an appropriate weighting. The same muon was then used more than once depending on the proportion of $\mu^+\mu^+$ and $\mu^-\mu^-$ events. For example, in the proton sample, the same μ^+ was used 35 times and the same μ^- 100 times, while in the sulphur sample, the numbers are 26 times and 22 times, respectively. A check of the method was made by comparing the dimuon mass, transverse momentum and rapidity distributions for the mixed like-sign sample with those of the measured like-sign sample; this leads to a χ^2/degree of freedom = 1608/1579 = 1.02, combining the p–W and S–W data. The overall normalization for the unlike-sign combinatorial background constructed by this procedure was given by real like-sign events via equation (1). More details and references concerning the combinatorial background can be found in [17, 18].

3.9 Absorber background

A different background of true muon pairs, contributing mainly to the low mass region, is the dilepton production in the hadron absorber by two sources: interacting hadrons and projectile fragments from the primary interaction in the target [18, 19]. The cuts described above on the Z-coordinate of the point of closest approach removed a large part of this background.

The spectral shape and the absolute rate of the remaining absorber background was estimated using a generator describing the hadron production in the target and subsequent dimuon production in the absorber. The primary hadron production simulation was based on the $dN_{charged}/d\eta$ measured by the HELIOS/2 collaboration [20] and a rapidity-dependent gaussian p_T distribution centered at the $\pi - p$ center of mass rapidity with an average value of 0.365 GeV/c and a width of 3 GeV/c. The hadron was tracked until its interaction in the absorber. The generator parameters were tuned to describe the experimental data taken in special runs with π beams at 25, 50 and 100 GeV/c impinging on the front face of the absorber.

The second source contributing to this type of background comes from non-interacting projectile nucleons ("fragments"). The number of fragment nucleons depends on the multiplicity class (centrality). The estimation of this background is based on the fits to distributions measured in a special run of 200 GeV/c protons hitting the tungsten plug, scaled by $A^{2/3}$ [21], like the inelastic hadronic cross section.

Since the reconstruction algorithm for muon pairs assumes the origin of the pair at the target, the reconstructed polar angles of pairs produced by the above processes are smaller than the true ones. Therefore, the effective dimuon mass and p_T of the absorber background are shifted towards lower values, and the rapidity to higher values. In the reconstructed dimuon mass spectrum this background appears therefore only below the ρ resonance and plays a small role in the analysis presented in this paper.

3.10 Normalization to charged particle reduction

In each multiplicity class, the sample of 0μ triggers was used to normalize the number of dimuons to the number of charged particles in the pseudorapidity interval $3.5 < \eta < 5.2$. The $\mu\mu/charged$ ratios were calculated at the trigger level, so that the multiplicity trigger acceptances cancelled. The yield of muon pairs normalized to the charged particle multiplicity is defined as:

$$\left(\frac{\mu\mu_{reconstructed}}{charged(3.5<\eta<5.2)}\right)_{trig,mult} = \frac{1}{< M_{trig,mult} >}\frac{F_{2\mu,trig}}{F_{0\mu,trig}}\frac{W^{corr}_{trig,mult}}{N^{corr}_{trig,mult}}$$

where

$trig$ = trigger type
$mult$ = multiplicity class
$< M_{trig,mult} >$ = average charged multiplicity ($3.5 < \eta < 5.2$)
$F_{2\mu,trig}, F_{0\mu,trig} = 2\mu$ and 0μ dead time correction factors
$N^{corr}_{trig,mult} = 0\mu$ triggers corrected for downscaling per beam
$W^{corr}_{trig,mult}$ = sum of 2μ weights due to acceptance corrected for downscaling per beam

The events with a cut on the multiplicity in the H1-hodoscope in the 2μ trigger were corrected for the missing triggers class-by-class using the sample with no H1 cut. The corrections were about 5% for the proton runs and 4–8% for the different sulphur multiplicity classes.

The results of the various triggers contributing to each multiplicity class were combined using weights corresponding to the overall errors of each trigger, including the errors of $< M_{trig,mult} >$, $F_{2\mu,trig}, F_{0\mu,trig}$, $N^{corr}_{trig,mult}$, $W^{corr}_{trig,mult}$. The point-to-point errors of individual mass bins were calculated from corresponding parts of $W^{corr}_{trig,mult}$. The error on the overall normalization is determined by the errors of the quantities $< M_{trig,mult} >$, $F_{2\mu,trig}, F_{0\mu,trig}$, $N^{corr}_{trig,mult}$, H1 cut corrections and the background estimation, taking into account the correlations.

3.11 The fits to the resonances

The dimuon mass spectra were fitted between 0.3 and 3.6 GeV/c^2 by the function

$$F(m) = P_1\left[0.6BW_\rho(m) + G_\omega(m) + P_2 G_\phi(m)\right] + P_3 PSI(m) + C(m)$$

where G_i are gaussians describing the ω and ϕ meson peaks, BW_ρ a p-wave Breit-Wigner function [22, 23], $PSI(m)$ a GEANT-determined J/Ψ line shape and $C(m)$ an empirical function describing the continuum. The constant 0.6, representing $(\sigma B_{\mu\mu})_\rho\,(\sigma B_{\mu\mu})_\omega$, was determined using $\sigma(\rho) = \sigma(\omega)$, as measured in p–p interactions [7], and the dimuon branching ratios, $B_{\mu\mu}$, from the Particle Data Group [24]. The results of this paper are not sensitive within errors to this assumption: a variation of 20% in $\sigma(\rho)/\sigma(\omega)$ results in a $\pm 3\%$ change in the results.

The Breit-Wigner function $BW_\rho(m)$ has a mass-dependent width. Relative to $\pi\pi$, the $\mu\mu$ partial width has an additional m^{-4} factor from the photon propagator suppressing the high mass shoulder of the Breit-Wigner function. The ρ meson shape in the dimuon mass spectrum was taken as:

$$BW_\rho(m) = \sigma(m)\frac{\pi^{-1}m^2\Gamma_{\rho\to\mu\mu}(m)}{\left(m^2 - m_\rho^2\right)^2 + m^2\Gamma^2_{\rho\to\pi\pi}(m)} \qquad (2)$$

where

$$\Gamma_{\rho\to\mu\mu}(m) = \frac{k}{k_0}\frac{\left(2m_\mu^2 + m^2\right)}{\left(2m_\mu^2 + m_\rho^2\right)}\frac{m_\rho^6}{m^6}\Gamma^0_{\rho\to\mu\mu}$$

and

$$\Gamma_{\rho\to\pi\pi}(m) = \left(\frac{k}{k_0}\right)^3\left(\frac{m_\rho}{m}\right)^2\Gamma^0_{\rho\to\pi\pi}$$

$$k = \sqrt{0.25m^2 - m_\mu^2} \text{ and } k_0 = \sqrt{0.25m_\rho^2 - m_\mu^2}$$

and $\sigma(m)$ is the cross section for the production of a stable particle with mass m (summed over all spin states).

The functional form of this cross section was found in analogy with the approach used for ρ meson searches in the $\pi\pi$ channel, where it is assumed to behave like the nonresonant background under the resonance. To avoid double counting the final state phase space (see e.g. [22]), we used

$$\sigma(m) = PS(m)\frac{m}{k_\pi} \qquad (3)$$

where $PS(m)$ is the uncorrelated $\pi\pi$ spectrum. The QGSM model [25] for p–p interactions at 200 GeV/c was used to obtain the form of $PS(m)$ for which the following parametrization was found to give a good description:

$$PS(m) = \left(\frac{k_\pi}{m}\right)^\beta \exp\left(ak_\pi + bk_\pi^2\right)$$

$$k_\pi = \sqrt{0.25m^2 - m_\pi^2}\,,$$

$\beta = 0.5725$, $a = -4.5729$ and $b = 0.3130$. In order that $PS(m)$ could be defined also below the $\pi\pi$ threshold mass, the pion mass was replaced with muon mass. Within errors, the results of this paper are also not sensitive to these assumptions.

Equation (2) was convoluted with the experimental resolution.

The mean masses of the ω and ϕ resonances were fixed at their nominal values, while the gaussian variances were

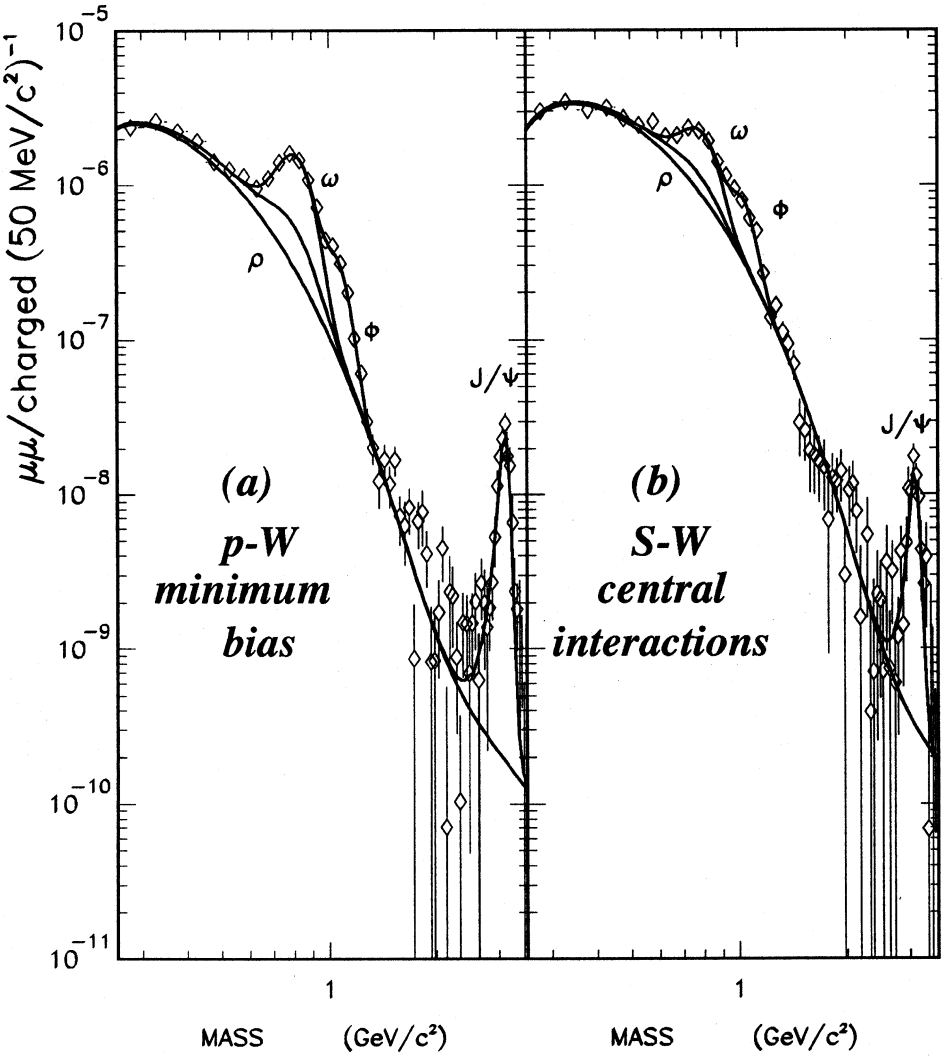

Fig. 6. Dimuon mass spectra for **a** minimum bias p–W and **b** central S–W interactions with fits and individual contributions superimposed. The J/Ψ and ρ contributions have been added to the continuum, followed by the ω contribution and, finally, the ϕ contribution. The log mass scale was chosen to emphasize the ρ, ω, ϕ region

Table 2. Centrality dependence of vector mesons relative to charged particle prodution. B refers to the relevant resonance $\mu\mu$ branching fraction

projectile participants	$B\sigma_\phi/\left(B\sigma_\rho + B\sigma_\omega\right)$	$B\sigma_\phi/\sigma_{charged}\ \times 10^6$	$\left(B\sigma_\rho + B\sigma_\omega\right)/\sigma_{charged}\ \times 10^6$
1	0.138 ± 0.009	0.97 ± 0.06	7.03 ± 0.17
14.5	0.224 ± 0.082	1.88 ± 0.65	8.32 ± 2.34
22.7	0.254 ± 0.086	1.64 ± 0.50	6.44 ± 1.30
26.6	0.217 ± 0.032	1.72 ± 0.23	7.92 ± 0.63
29.4	0.318 ± 0.033	2.15 ± 0.18	6.77 ± 0.47
30.6	0.317 ± 0.046	2.15 ± 0.24	6.75 ± 0.61

equal to the experimental resolution. The results of the fits indicate that the experimental resolution is well understood. The fits were not improved by considering the resonance masses as free parameters.

The function $PSI(m)$ was determined between 2.5 and 3.5 GeV/c^2 by a full GEANT simulation.

Equation (4) represents the continuum function chosen for its behavior at threshold and high mass (i.e. Drell-Yan-like).

$$C(m) = \left(P_4 e^{P_5 m} + \frac{P_6}{m^3} e^{P_7 m}\right)\left(1 - \frac{2m_\mu}{m}\right)^{P_8} \qquad (4)$$

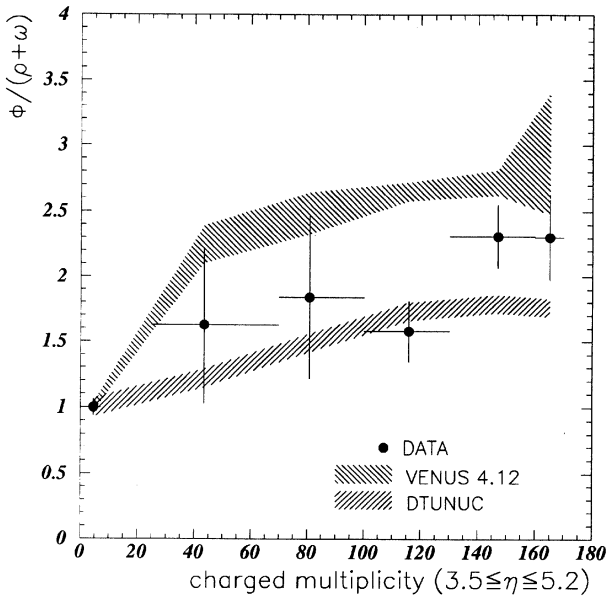

Fig. 7. The $\phi/(\rho+\omega)$ ratio, normalized to the proton point, vs. the charged multiplicity. A comparison with the predictions of VENUS 4.12 and DTUNUC 1.02 is made

The smoothness of this function is justified by the experimental mass resolution, Sect. 3.6. As examples of the data and the fits, Fig. 6 displays the minimum bias p–W and central S–W dimuon mass spectra with the fits and the individual contributions superimposed: continuum, J/Ψ, ρ, ω and ϕ.

4 Results

In the following, we present the dependence on centrality, transverse momentum p_T and rapidity y of vector meson production as well as the ratio $B\sigma_\phi/(B\sigma_\rho + B\sigma_\omega)$ where B is the relevant resonance branching fraction into $\mu\mu$. Furthermore, we present some results on J/Ψ production. In general, we have normalized our results to the charged particle production in the fixed pseudorapidity interval $3.5 < \eta < 5.2$.

The measured projectile participant and multiplicity dependence of the $B\sigma_\phi/(B\sigma_\rho + B\sigma_\omega)$ ratio is given in Table 2 and Fig. 7, respectively. The data in Fig. 7 have been normalized to the proton value. The horizontal error bars reflect the binning of the charged multiplicity. The ratio $B\sigma_\phi/(B\sigma_\rho + B\sigma_\omega)$ clearly increases with multiplicity with some indication, at the two sigma level, of an increase with centrality in S–W interactions.

For proton and central sulphur interactions, three p_T and three y bins were considered. Note that these bins refer only to the dimuons, not to the charged particles used for the normalization. The ratios evaluated in different intervals of transverse momentum are presented in Table 3 and show an enhancement of the ratio $B\sigma_\phi/(B\sigma_\rho + B\sigma_\omega)$ from proton to central sulphur data, with no clear dependence on p_T. On the other hand, the rapidity results (Table 4) show that this enhancement increases strongly with rapidity. It is expected that the more massive resonance will extend less in rapidity; only a detailed model, beyond the scope of this paper, can untangle this kinematic effect to uncover the dynamics.

Table 3. Transverse momentum dependence of $B\sigma_\phi/(B\sigma_\rho + B\sigma_\omega)$ for minimum bias p–W and central S–W collisions. B refers to the relevant resonance $\mu\mu$ branching fraction

	central S–W	p–W	(S–W)/(p–W)
$p_T \leq 0.35$	0.266 ± 0.041	0.137 ± 0.017	1.94 ± 0.38
$0.35 < p_T \leq 0.6$	0.204 ± 0.042	0.145 ± 0.015	1.41 ± 0.32
$0.6 < p_T$	0.315 ± 0.032	0.136 ± 0.013	2.32 ± 0.32

Table 4. Rapidity dependence of $B\sigma_\phi/(B\sigma_\rho + B\sigma_\omega)$ for minimum bias p–W and central S–W collisions. B refers to the relevant resonance $\mu\mu$ branching fraction

	central S–W	p–W	(S–W)/(p–W)
$y \leq 3.9$	0.314 ± 0.031	0.232 ± 0.017	1.35 ± 0.17
$3.9 < y \leq 4.4$	0.289 ± 0.040	0.078 ± 0.009	3.71 ± 0.67
$4.4 < y$	0.202 ± 0.021	0.038 ± 0.008	5.32 ± 1.25

Table 5. Rapidity dependence of $B\sigma_\phi/\sigma_{charged}$ for minimum bias p–W and central S–W collisions. B refers to the $\phi \to \mu\mu$ branching fraction

rapidity region	central S–W $\times 10^6$	p–W $\times 10^6$	(S–W)/(p–W)
$y < 3.9$	1.58 ± 0.13	0.83 ± 0.05	1.90 ± 0.19
$3.9 < y \leq 4.4$	0.50 ± 0.15	0.17 ± 0.02	2.94 ± 0.94
$4.4 < y$	0.20 ± 0.02	0.052 ± 0.011	3.85 ± 0.90

To study separately the ϕ and $(\rho+\omega)$ behavior, we have determined the $B\sigma_\phi/\sigma_{charged}$ and $(B\sigma_\rho + B\sigma_\omega)/\sigma_{charged}$ ratios as a function of centrality (Table 2 and Fig. 8). The values in the figures have been normalized to the proton point. We observe that there is an increase in the $B\sigma_\phi/\sigma_{charged}$ ratio, while the $(B\sigma_\rho + B\sigma_\omega)/\sigma_{charged}$ ratio remains constant. We have also determined the rapidity variation of $B\sigma_\phi/\sigma_{charged}$ (Table 5) and $(B\sigma_\rho + B\sigma_\omega)/\sigma_{charged}$ (Table 6). In all cases, there is a strong decrease at higher rapidity but this decrease is quite different for proton and central sulphur interactions, depending on the resonance. In particular, the ϕ falls about half as much in S–W than in p–W interactions, while the $\rho + \omega$ falls twice as fast for S–W than for p–W interactions. Differences between the p–W and S–W rapidity variations for a given resonance are expected due to the difference in the position of the rapidity distribution peak between the two reactions; again, a detailed model is needed to distinguish the kinematics from the dynamics.

In [18], we will present the m_T distributions for the different resonance mass regions and compare the inverse slope parameters with those of the continuum regions.

NA38 measurements [26] of the ratio $B\sigma_\phi/(B\sigma_\rho + B\sigma_\omega)$ performed at relatively high transverse momentum, complementary to our experiment, have shown an increase

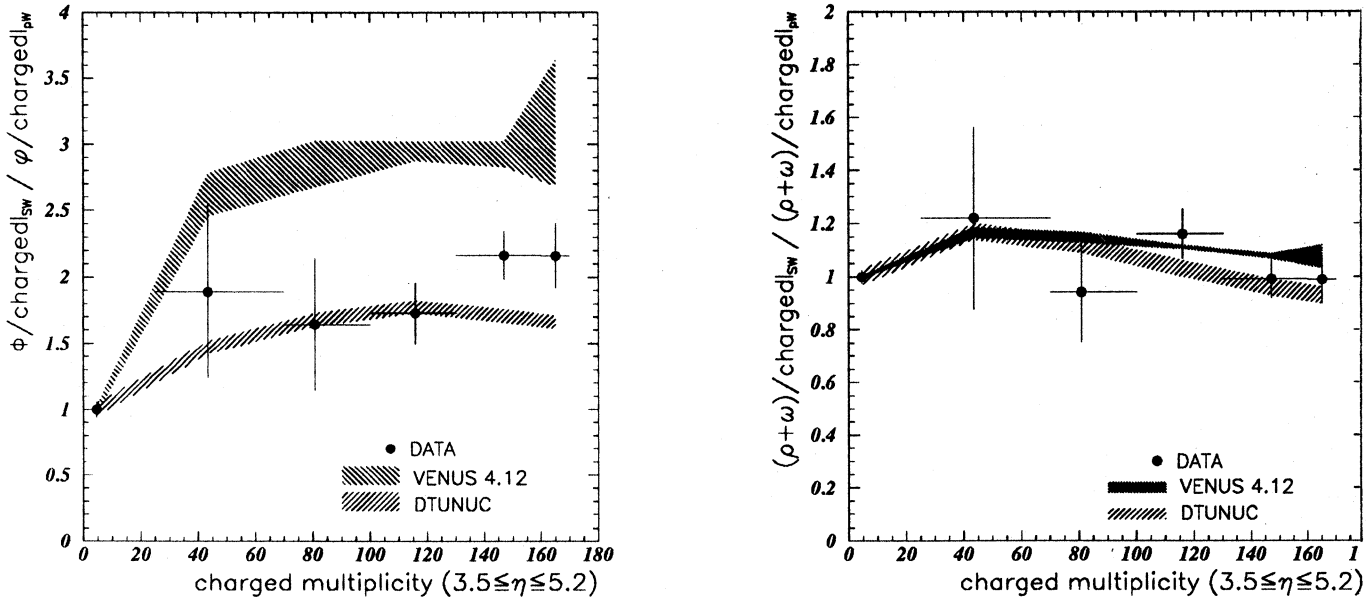

Fig. 8. The ϕ/charged and $(\rho+\omega)$/charged ratio, normalized to the proton point, vs. the charged multiplicity. A comparison with the predictions of VENUS 4.12 and DTUNUC 1.02 is made

Table 6. Rapidity dependence of $(B\sigma_\rho + B\sigma_\omega)/\sigma_{charged}$ for minimum bias p–W and central S–W collisions. B refers to the relevant resonance $\mu\mu$ branching fraction

rapidity region	central S–W $\times 10^6$	p–W $\times 10^6$	(S–W)/(p–W)
$y < 3.9$	5.04 ± 0.37	3.47 ± 0.14	1.45 ± 0.12
$3.9 < y \leq 4.4$	1.56 ± 0.49	2.15 ± 0.08	0.72 ± 0.23
$4.4 < y$	1.00 ± 0.08	1.37 ± 0.05	0.73 ± 0.06

Table 7. Ratio of $B\sigma_{J/\Psi}/\sigma_{charged}$ production for central S–W interactions relative to minimum bias p–W interactions as a function of centrality. B refers to the $J/\Psi \to \mu\mu$ branching fraction

Nr. of proj. part. mean	S–W/p–W $B\sigma_{J/\Psi}/\sigma_{charged}$
26.6	0.66 ± 0.14
29.4	0.65 ± 0.10
30.6	0.71 ± 0.15

relative to centrality which is consistent with our result; their result corresponds approximately to our first rapidity bin combined with our last transverse momentum bin.

The behavior of increased ϕ production has also to be seen in the context of increased production in heavy ion interactions of other strange particles, like kaons and strange baryons. However, for a quantitative interpretation of the observed enhancement, our dimuon acceptance and kinematic effects between p–W and S–W collisions have to be taken into account. We have attempted this for two specific models and will present our results in the next section of this paper.

Table 8. Rapidity dependence of $B\sigma_{J/\Psi}/\sigma_{charged} \times 10^7$ for minimum bias p–W and central S–W collisions. B refers to the $J/\Psi \to \mu\mu$ branching fraction

rapidity region	central S–W	p–W
$y \leq 3.9$	0.57 ± 0.07	1.03 ± 0.09
$3.9 < y \leq 4.4$	0.095 ± 0.020	0.11 ± 0.02
$4.4 < y$	0.0092 ± 0.0053	0.0098 ± 0.0062

The $B\sigma_{J/\Psi}/\sigma_{charged}$ ratio in our kinematic region is $(1.20 \pm 0.10)10^{-7}$ in p–W interactions. Table 7 gives the dependence on centrality relative to p–W interactions and qualitatively confirms the suppression seen by [27]. Note however that our normalization to charged particles (produced by soft processes) differs from their normalization to the continuum (produced by hard processes).

For completeness, Table 8 shows the rapidity dependence of J/Ψ production in minimum bias p–W and central S–W interactions.

We emphasize that our vector meson results are presented as ratios in a fixed rapidity window, sometimes with respect to each other and sometimes with respect to charged particles in a similar but not identical pseudorapidity window. The A^α-dependence of particle production usually depends on Feynman's x_F with a specific $\alpha(x_F)$ for each particle; for example, see [28, 29]. Therefore, the interpretation of our results must necessarily entail a comparison with models.

5 Comparison with models and discussion

Quantitative comparisons were made with two physics generators, DTUNUC 1.02 [30] and VENUS 4.12 [15], each

based on the dual parton model (DPM) [31] with the addition of an intranuclear cascade model. Version 4.12 of VENUS was used (as opposed to version 3.11) since it keeps both the parent vector meson as well as its decay products which are necessary for the normalization to charged particles. The naive treatment of intranuclear cascade processes overestimates particle yields in particular in the region of high hadron density where independent binary interactions are implausible. One way to modulate the treatment is by the introduction of a formation zone which suppresses the cascading of high-energy secondaries. This is introduced via a simple formation time concept [30]. Another way is to introduce cluster formation and decay [15]. In either case, the treatment is ad-hoc.

Within the DPM, the high-energy projectile undergoes a multiple scattering process. Particles are produced by the fragmentation of two colorless parton-parton chains constructed from valence quarks and sea-q$\overline{q}$ pairs associated with the interacting particles. In this model, the number of chains with sea-quarks at their ends grows with the complexity of the target and projectile nuclei. For example, in p–p interactions at our energies, there are no chains with sea quarks to first order, while they exist in p-A collisions, increasing with A. In particular, since the masses of these chains are in the GeV energy range, there is no reason to suppose strange quark suppression. Therefore an SU(3) flavor symmetry is possible for these sea-quarks. This mechanism leads to a rise in the relative yield of strange particles as the final state multiplicity increases.

The predictions of the two models, normalized to the proton value, are shown on Fig. 7 and Fig. 8. Relative to the data, VENUS predicts a more rapid rise of $\phi(\rho+\omega)$ as a function of centrality. The discrepancy is due to the larger rise in $\phi/chgd$ while the $(p+\omega)/chgd$ ratio is well reproduced. The DTUNUC predictions are more consistent with the data.

For VENUS, the data are about 1.5–2 times the absolute predictions (not shown) of $(\rho+\omega)/chgd$ and $\phi/chgd$ ratios while the $\phi/(\rho+\omega)$ ratios are quite consistent with the data, except that the proton data point is about 1.5 times the prediction. The latter seems due to a larger underestimation of the $\phi/chgd$ compared to the data than $(\rho+\omega)/chgd$ in p–W interactions. It should be pointed out that VENUS overestimates the charged particle production as compared to data [32]. The absolute predictions of $(\rho+\omega)/chgd$ and $\phi/chgd$ ratios by DTUNUC are similarly low but somewhat independent of projectile.

Other models predict that the ratio $\phi/(\rho+\omega)$ should rise either by about 6–10 [8] or 1.8 [9] over its $p-p$ value, quite higher or somewhat lower than our data, respectively. The prediction [33] that this rise appears only at high p_T is invalidated by the results of this paper.

6 Conclusions

In this paper we have presented a measurement of $\rho+\omega$, ϕ and J/ψ vector meson production in p–W and S–W interactions at 200 GeV/c/nucleon for forward rapidities, the rapidity threshold depending on the transverse mass. Within this kinematic range, the ϕ resonance is enhanced in heavy ion collisions by a factor of about two relative to the other low mass resonances. As a function of the charged particle multiplicity in our acceptance, the $\rho+\omega$ combination is unchanged, the ϕ is enhanced and the J/Ψ is suppressed.

From the comparisons to the DTUNUC and VENUS models, we conclude that there is no compelling evidence in our data on vector meson production for physics processes not already included in these models, such as the quark-gluon plasma (which could nonetheless exist at some level). To make this a firmer conclusion, these models should reproduce the unusual multiplicity dependence of ϕ production measured in pBe interactions at 450 GeV/c [12] as well as the measurements of other particles containing strange quarks, such as hyperons.

Acknowledgements. The HELIOS/3 collaboration wishes to thank the staff of the PS-SPS accelerator complex for their outstanding performance. The valuable contributions of the technical staff of CERN and the collaborating institutes are gratefully acknowledged. We are grateful for support by the Direction des Sciences de la Matiére (CEA, France) and the Istituto Nazionale di Fisica Nucleate of Italy.

References

1. R.Pisarsky: Phys. Lett. **B110** (1982) 155
2. G.E.Brown and M.Rho: Phys. Reports. **269** (1996) 3
3. T.Hatsuda and S.-H.Lee, Phys.Rev. **C46** (1992) 34.
4. B.F'riman, Nucl.Phys. **A610** (1996) 358c, and many references therein
5. J.Rafelsky and B. Muller: Phys. Lett. **B48** (1982) 1066 and J. Rafelsky: Nucl. Phys. A418 (1984) 215
6. A. Shor: Phys. Rev. Lett. **54** (1985) 1122
7. M.Aguilar-Benitez et al. (NA27): Z. Phys. **C50** (1991) 405
8. P. Koch, U. Heinz, J. Pisut: Phys. Lett. B243 (1990) 149; Z. Phys. **C47** (1990) 477
9. H. Sorge et al.: Z. Phys. **C59** (1993) 85
10. more details are to be found in F. Martelli: Produzione di mesoni vettoriali in interazioni S–W e p–W a 200 GeV/nucleone, Tesi del Dottorato di Ricerca in fisica, V Ciclo, (1993)
11. P. Giubellino et al.: Nucl. Instr. Meth. **A275** (1989) 89
12. T. Akesson et al.: Z. Phys. **C68** (1995) 47
13. I. Kralik: Intermediate Mass Dimuon Production in p–W and S–W Collisions at 200 GeVIcIA, PhD Thesis, Inst. of Experimental Physics, Kogice, 1995, unpublished. See in particular Figure 4.12
14. T. Akesson et al.: Nucl. Phys. **B333** (1990) 48
15. K. Werner: Phys. Rep. **232** (1993) 88 and references therein
16. B. Andersson, G. Gustafsson and B. Nilsson-Almqvist: Nucl. Phys. **B281** (1987) 289
17. J. Bystricky et al.: to be submitted for publication to Nucl. Instr. Methods
18. "Excess of continuum dimuon production at masses between threshold and the J/XP in S–W interactions at 200 GeV/c/nucleon", A.L.S.Angelis et al.: to be submitted for publication to Zeit. fur Phys

19. G. London: HELIOS/3 note 83
20. M. Masera: 24th Rencontres de Moriond, New results in hadronic interactions, J. Tran Thanh Van editor, Editions Frontieres (1989) 477
21. G. Baroni et al.: Nucl. Phys **A531** (1991) 691
22. J.D.Jackson: 11 Nuovo Cimento **34** (1964) 1644
23. Z.Y.Fang, G.Lopez Castro and J.Pestieau: Use and Misuse of the Breit-Wigner Formula. Preprint **UCL-I** p_T **87-07**. May 1987
24. Review of Particle Properties, Phys. Rev. **D50** (1994) 1173
25. N.S.Amelin, K.K.Gudima and V.D.Toneev: NATO ASI series B: Physics **2116** (1989) 473, and preprint **GSI 89-52**
26. C. Baglin et al.: Phys. Lett. **B272** (1991) 449
27. C. Baglin et al.: Phys. Lett. **B270** (1991) 105
28. W. Geist: Nucl- Phys. **A525** (1991) 149c
29. R. Salmeron: Nucl. Phys. **A566** (1994) 199c
30. J.Ranft: SSC-re'port 150 (1987) 1 H.-J.M6hring, J.Ranft: Z. Phys. **C52** (1991) 6431 I.Kawrakow, H.-J.Möhring, J.Ranft: Z. Phys. **C56** (1992) 115
31. A. Capella et al.: Nucl. Phys. **B241** (1984) 75
32. T. Akesson et al.: Nucl. Phys. **B333** (1989) 1
33. F. Grassi and H. Heiselberg: Phys. Lett. **B267** (1991) 1